Subaru Hyper Suprime-Cam revisits the large-scale environmental dependence on galaxy morphology over 360 deg² at z=0.3–0.6

Rhythm Shimakawa 1,2*† , Takumi S. Tanaka 1,2 , Seiji Toshikage 3 and Masayuki Tanaka 1

- ¹National Astronomical Observatory of Japan (NAOJ), National Institutes of Natural Sciences, Osawa, Mitaka, Tokyo 181-8588, Japan
- ²Department of Astronomy, School of Science, The University of Tokyo, 7-3-1 Hongo, Bunkyo-ku, Tokyo 113-0033, Japan
- ³Astronomical Institute, Tohoku University, 6-3, Aramaki, Aoba, Sendai, Miyagi, 980-8578, Japan
- *E-mail: rhythm.shimakawa@nao.ac.jp (RS)

Received; Accepted

Abstract

This study investigates the role of large-scale environments on the fraction of spiral galaxies at z=0.3-0.6 sliced to three redshift bins of $\Delta z=0.1$. Here, we sample 276 220 massive galaxies in a limited stellar mass of 5×10^{10} solar mass ($\sim M^*$) over 360 deg², as obtained from the Second Public Data Release of the Hyper Suprime-Cam Subaru Strategic Program (HSC-SSP). By combining projected two-dimensional density information (Shimakawa et al. 2021) and the CAMIRA cluster catalog (Oguri et al. 2018), we investigate the spiral fraction across large-scale overdensities and in the vicinity of red sequence clusters. We adopt transfer learning to significantly reduce the cost of labeling spiral galaxies and then perform stacking analysis across the entire field to overcome the limitations of sample size. Here we employ a morphological classification catalog by the Galaxy Zoo Hubble (Willett et al. 2017) to train the deep learning model. Based on 74 103 sources classified as spirals, we find moderate morphology-density relations on ten comoving Mpc scale, thanks to the wide-field coverage of HSC-SSP. Clear deficits of spiral galaxies have also been confirmed, in and around 1136 red sequence clusters. Furthermore, we verify whether there is a large-scale environmental dependence on rest-frame u-r colors of spiral galaxies; however, such a tendency was not observed in our sample.

Key words: galaxies: general — galaxies: evolution — galaxies: clusters: general — galaxies: statistics

1 Introduction

Physical mechanisms of environmental impacts on galaxy formation and evolution, and even the very existence of such effects, have been long-standing controversial topics, depending on such an evolutionary phase, a cosmic time, or an environmental scale (e.g., reviews by Boselli and Gavazzi 2006; Blanton and Moustakas 2009; theoretical work by Davis et al. 1985; Dekel and Silk 1986; Moore et al. 1998; White and Frenk 1991; Kereš et al. 2005; Bekki and Couch 2011; Somerville and Davé 2015; Joshi et al. 2020; Donnari et al. 2021). For example, many studies have reported a close color—magnitude relationship, called

[†] NAOJ Fellow

red sequence, since redshift ~ 2 or less (de Vaucouleurs 1961; Visvanathan and Sandage 1977; Butcher and Oemler 1984; Bower et al. 1992; Bower et al. 1998; Terlevich et al. 2001; Gladders and Yee 2005; White et al. 2005; Kodama et al. 2007; Cooper et al. 2007; Muzzin et al. 2008; Mei et al. 2009; Rykoff et al. 2014; Oguri et al. 2018). Such color dependencies on the local galaxy over-density have been verified in more diversified environments via extensive wide-field surveys covering more than a hundred square degrees (Balogh et al. 2004; Tanaka et al. 2005; Baldry et al. 2006; Skibba et al. 2009; Peng et al. 2010; Alpaslan et al. 2015; Costa-Duarte et al. 2018). Indeed, less active star formations of cluster galaxies have been detected in various observations, which suggests that dense environments induce star formation quenching (Kauffmann et al. 2004; Poggianti et al. 2006; Wetzel et al. 2012; Wetzel et al. 2013; Muzzin et al. 2014; Old et al. 2020). Environmental quenching is often regarded as a quenching process, together with mass-dependent star formation quenching (Peng et al. 2010; Grützbauch et al. 2011; Peng et al. 2012).

The morphology-density relation, which is the primary focus of this paper, is a more contentious research topic than the environmental dependence of galaxy colors, which refers to the increase in disk early-type (S0) galaxies in dense regions, at the cost of a fraction of spiral galaxies (Dressler 1980; Larson et al. 1980; Dressler et al. 1997; Couch et al. 1998; Goto et al. 2003a; Smith et al. 2005; Postman et al. 2005; Capak et al. 2007; Guzzo et al. 2007; van der Wel 2008; Poggianti et al. 2009; Tasca et al. 2009; Cappellari et al. 2011; Lietzen et al. 2012; Houghton et al. 2013; Fogarty et al. 2014). The relationship apparently indicates a morphological transition of star-forming galaxies to the early-type galaxies owing to environmental effects like ram pressure stripping and gas strangulation (Moran et al. 2007; Wolf et al. 2009; Kovač et al. 2010; Vulcani et al. 2011). However, previous studies have reported that such an apparent environmental dependence tends to almost disappear at a fixed stellar mass, especially at the high mass end, thus suggesting that the mass would primarily control such an observational trend (e.g. Holden et al. 2007; Bamford et al. 2009, and see also Brough et al. 2017; Veale et al. 2017; Greene et al. 2017 for the kinematic morphology-density relation in early-type galaxies).

Moreover, quite importantly, a significant fluctuation in the environmental dependence would exist, just as there is a great diversity of galaxy clusters (Rood and Sastry 1971; Butcher and Oemler 1984; Goto 2005; Hashimoto et al. 2019). Recent wide-field deep legacy surveys have determined more than a thousand cluster samples by systematic cluster search out to $z \sim 1$, e.g., CAMIRA (Oguri et al. 2018), AMICO (Maturi et al. 2019), and X-CLASS

(Koulouridis et al. 2021). Besides, we have free access to the wide-field projected density map at z < 1 over 360 deg² (Shimakawa et al. 2021). These libraries that sufficiently cover the sample size and survey volume will enable us to obtain a more systematic perspective on environmental dependence across a formation history of the large-scale structure.

Therefore, this motivates us to revisit the morphologydensity relation using large data-sets based on wide-field deep data. Specifically, we obtain the sample from the Second Public Data Release of the Hyper Suprime-Cam Subaru Strategic Program (Aihara et al. 2019; hereafter referred to as the HSC-SSP PDR2), as well as the density map (Shimakawa et al. 2021) and CAMIRA cluster catalog (Oguri et al. 2018), both of which are based on the HSC-SSP PDR2 library (§2). Furthermore, this research employs a novel approach, transfer learning (Bozinovski and Fulgosi 1976; Pratt 1993), to achieve an effective search of spiral galaxies from big data (§3). Transfer learning is a machine-learning technique occasionally used for the classifications of galaxy mergers (Ackermann et al. 2018) and radio galaxies (Tang et al. 2019), including the application of a visual morphology classification to another survey (Domínguez Sánchez et al. 2019). Based on the deep learning classification, we investigate the environmental dependence of spiral fractions on 10 comoving Mpc (co-Mpc) scale and in the vicinity of galaxy clusters (§4). This study primarily focuses on such a large-scale environmental effect by taking advantage of the wide-field coverage (360 deg²) and owing to photometric redshift errors on the backside. Finally, we discuss obtained results and summarize this research in the last section (§5 and §6).

Similar to our previous work (Shimakawa et al. 2021), this study adopts the AB magnitude system (Oke and Gunn 1983) and the Chabrier (2003) initial mass function. We also assume cosmological parameters, $\Omega_M=0.279$, $\Omega_{\Lambda}=0.721$, and h=0.7, in a flat lambda cold dark matter model, which are consistent with those from the WMAP nine-year data (Hinshaw et al. 2013). When referring to our figures or tables, we designate their initials by capital letters (e.g., Fig. 1, Table 1, Section 1) to avoid confusion with those in the literature (e.g., fig. 1, table 1, or section 1).

2 Data

This section overviews an original sample obtained from the HSC-SSP PDR2, which is applied in the density measurement in our previous work (Shimakawa et al. 2021). We then examine how to prepare an imaging data-set for selecting spiral galaxies from our sample.

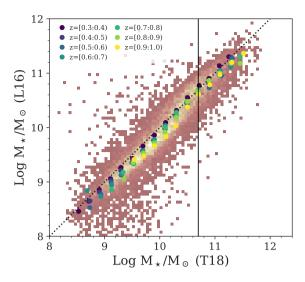


Fig. 1. Comparisons of stellar mass estimates of i < 23 galaxies at z = [0.3:1.0) by (x-axis) Tanaka et al. (2018), based on HSC grizy bands with those by (y-axis) Laigle et al. (2016), which use all photometric bands available in the COSMOS field (Scoville et al. 2007). The median values are depicted by the circles (colors of the symbols vary depending on the redshift bin as denoted in the legend). The black solid vertical line indicates the stellar mass limit ($\rm M_{\star} = 5 \times 10^{10} \ M_{\odot}$) determined in this work.

2.1 HSC-SSP PDR2

This work is based on data, all of which have been available in the public database of the HSC-SSP PDR2¹ since May 30, 2019 (Aihara et al. 2019). The database includes all data taken from March 2014 to January 2018 (refer to Aihara et al. 2019, table 2 for further details) with the Hyper Suprime-Cam on the 8.2 m Subaru Telescope (Miyazaki et al. 2018; Furusawa et al. 2018; Kawanomoto et al. 2018; Komiyama et al. 2018). Using the database, we can access the science-ready source catalog and reduced fits data generated by the dedicated pipeline termed hscPipe (Bosch et al. 2018).

Throughout this study, we employ only luminous galaxies in a limited stellar mass of $M_{\star} = 5 \times 10^{10}$ solar mass at a photometric redshift range of z = [0.3:0.6). The sample is originally based on approximately eight million i-band magnitude limited (< 23 mag) sources of the study by Shimakawa et al. (2021). They are detected in all HSC bands (qrizy) with more than five sigma detections in the cmodel measurement (see Bosch et al. 2018, §4.9.9 and Abazajian et al. 2004, §3.1 for details of the cmodel magnitude). Suspicious detections are excluded using the following flags (is False) on the HSC-SSP PDR2database: pixelflags_edge, pixelflags_interpolatedcenter, pixelflags_saturatedcenter, pixelflags_crcenter, pixelflags_bad, pixelflags_bright_objectcenter, mask_s18a_bright_objectcenter,

and i_sdsscentroid_flag (Coupon et al. 2018; Aihara et al. 2019; Bosch et al. 2018, table 2).

Photometric redshifts and stellar masses of the sample are derived from Mizuki, a SED-based photo-z code (Tanaka 2015). The biweight dispersion of $\Delta z = |z_{\rm spec} - z_{\rm photo}|$ is ≤ 0.04 , and the outlier rate ($|\Delta z| > 0.15$) is ~ 0.1 for the HSC-SSP sources at i < 23 mag (see Tanaka et al. 2018, table 2 for more details). We solely utilize samples that satisfy the reduced chi-square $\chi_{\nu} < 5$ of the best-fitting model, following the recommendation in Tanaka et al. (2018), section 7. For the sample at redshift z = [0.4:0.5), we set a further selection threshold to minimize an uncertainty from a Balmer–Lyman break degeneracy. Since misclassified samples at $z \sim 3$ tend to exhibit very young ages (~ 1 Gyr) with high specific star-formation rates (> 1 Gyr⁻¹) in the Mizuki, we discard such sources.

In addition, we conduct a sanity check on the stellar mass measurement by Mizuki at z = [0.3:1.0) using only the grizy photometry available in HSC-SSP as compared to those by COSMOS2015 (Laigle et al. 2016), which are based on 34-band photometry (Fig. 1). The HSC-only measurement restricted to the optical regime generally tends to overestimate stellar masses of galaxies at higher redshifts $(z \gtrsim 0.6)$ and lower stellar masses $(\lesssim a \text{ few } 10^{10})$ solar mass). However, Fig. 1 shows that we can obtain logical values for massive galaxies at $z \lesssim 0.6$, whose restframe optical wavelength can be covered optimally by zyfilters. We therefore decide to adopt massive galaxies at z = [0.3:0.6), with stellar masses greater than 5×10^{10} solar mass, which approximately corresponds to the characteristic stellar mass at that redshift (Ilbert et al. 2010; Davidzon et al. 2017). There are 276 220 galaxies that meet these requirements. Such thresholds are also selected from the seeing limit perspective (FWHM = 0.7 arcsec). It is substantially challenging for the seeing-limited data to resolve the morphology of more compact (i.e., lower-mass) galaxies and higher-z sources.

2.2 Density map and galaxy cluster sample

We select an area of 360 \deg^2 from the HSC-SSP Wide layer (Aihara et al. 2019, see figure 1), where the projected 2D density maps are available (Shimakawa et al. 2021). In practice, the survey fields are organized by five large areas, one of which is illustrated in Fig. 2 as an example. Shimakawa et al. (2021) selected the survey area in an *i*-band limiting magnitude (5 σ) of point-spread-function (PSF) in two arcsec diameters deeper than 26 mag. They also discard problematic fields adversely affected by bright stars (<17.5 mag) at a rate of more than 50 percent (see section 2 in the literature). We verify that our mask cor-

¹ https://hsc-release.mtk.nao.ac.jp

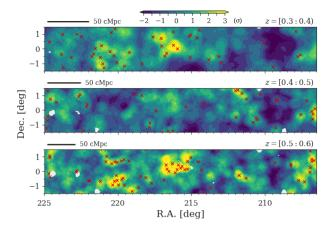


Fig. 2. Examples of the density map (see Shimakawa et al. 2021 for the full version). From top to bottom, projected two-dimensional overdensities at $z=[0.3:0.4), [0.4:0.5), {\rm and}\ [0.6:0.7), {\rm respectively}.$ The color map depicts the density excess in standard deviation $(\sigma_{\rm r=10Mpc}).$ The overdensity is measured for i-band magnitude limited galaxies (i<23) based on r=10 co-Mpc aperture. The red cross symbols indicate positions of the CAMIRA clusters at each redshift slice (Oguri et al. 2018). While the CAMIRA clusters generally follow the large-scale overdensities, there are some mismatch because measuring scales and tracers are different in the two density measurements (see Shimakawa et al. 2021 for more details).

rection provides the number density required at the target redshift range z=[0.3:0.6), which is consistent with that based on the COSMOS2015 catalog (Laigle et al. 2016). Detailed information on the density estimation can be found in Shimakawa et al. (2021), section 3.1. To derive the overdensity of our sample, we consider values of the density excess using r=10 co-Mpc apertures ($\sigma_{\rm r=10Mpc}$) in three redshift slices of $z=[0.3:0.4),\ [0.4:0.5),\ {\rm and}\ [0.5:0.6).$ Both the galaxy sample and density map are originally based on a study by Shimakawa et al. (2021). Hence, the survey areas are completely consistent with each other.

In addition, we employ a red sequence cluster catalog obtained from Oguri et al. (2018) to investigate spiral fractions of cluster neighborhoods. The cluster catalog was constructed based on the CAMIRA (Clusterfinding Algorithm based on Multi-band Identification of Red-sequence gAlaxies) algorithm (Oguri 2014). The program estimates the 3D richness of red sequence galaxies in a limiting stellar mass of $10^{10.2}$ M_{\odot} within one h^{-1} physical Mpc (see Oguri 2014 for more detailed information). We use their catalog correlating to the HSC-SSP PDR2, which includes the incremental update from the original version in the literature. We here adopt only cluster samples above the richness limit of 15, which roughly corresponds to the cluster virial mass of $\gtrsim 10^{14} \ h^{-1} \rm M_{\odot}$ (Oguri et al. 2018). Such red sequence cluster samples will enable us to revisit the well-known morphology-density relation (Dressler 1980) in and around galaxy clusters at intermediate redshifts in a more inclusive manner.

2.3 Image preparation

This research utilizes gray-scale images from i-band data, consisting of relatively homogeneous and better-seeing data (FWHM ~ 0.55 arcsec) than those in the other photometric bands (see e.g., Shimakawa et al. 2021, fig. 2). The HSC i-band filter captures the rest-frame 4400–6500 Å of our targets at z=[0.3:0.6). Beyond the technical reason above, we prefer to adopt the gray-scale than the multi-band colored image to avoid a color–morphology dependency (e.g., de Vaucouleurs 1961; Schawinski et al. 2014) that may produce a classification bias. We employ samples with seeing FWHM < 0.7 arcsec and then perform Gaussian smoothing for every data to match their seeing sizes to FWHM = 0.7 arcsec, based on the seeing information in the corresponding patch of the HSC-SSP PDR2 library.

We convert *i*-band data of the targets into the machine-friendly gray-scale images by following the form of the arcsinh stretch, $F(x) \equiv \operatorname{arcsinh}(x/\beta)$, proposed by Lupton et al. (1999); Lupton et al. (2004), where x is a flux count per pixel in the *i*-band, and β is the softening parameter (in this work, $\beta = 1 \times 10^{-3}$). The zero-point magnitude of the *i*-band data is scaled to 19 mag (default in hscMap²) from the original value in HSC-SSP (27 mag). A normalization formula is described as follows,

$$f(x) = \begin{cases} 0 & (x < m) \\ F(x-m)/F(M-m) & (m \le x \le M) \\ 1 & (M < x), \end{cases}$$
 (1)

where m is an undercut value ($m=5\times 10^{-5}$) and M represents an upper limit defined to be the maximum count within the central region of individuals (3×3 pixels) in this study. Subsequently, we cut out and convert the normalized data into the png format with the image size of (64×64) pixels (corresponding to 10.75×10.75 arcsec²), to turn the data cube into a deep learning model (§3.1). Examples of normalized images can be found in Fig. 6 and 7 in the next section.

3 Galaxy classification

In this section, we first introduce our machine-learning-based approach (§3.1) and explain how to train and validate the classification model by referencing it to the archive catalog, Galaxy Zoo Hubble (Willett et al. 2017) in §3.2. We then select spiral galaxies by applying the trained model to the normalized cutouts of the main targets (§3.3).

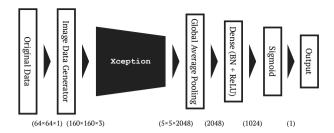


Fig. 3. Image illustration of our transfer learning model architecture where a two-class sigmoid classifier is attached to the Xception model with 36 convolutional layers (Chollet 2016). The parenthesized numbers indicate the size of the data cube in each process. "BN" means a batch normalization layer (Ioffe and Szegedy 2015).

3.1 Transfer learning

We applied transfer learning (see, e.g., Bozinovski and Fulgosi 1976; Pratt 1993 and a review by Tan et al. 2018) to select spiral galaxies from the entire sample. Transfer learning is a machine learning technique, where a model pre-trained on one domain is diverted to another task. Modern deep learning models preliminarily trained with large imaging data cubes can be considered experts of feature recognition, delivering superior performance on galaxy images by including an adapted classifier, even if they are total strangers to the models. The major advantage of adopting transfer learning is that we can significantly reduce the sample size of the training data-set while keeping a robust classification accuracy. This approach has recently garnered increasing applications in the field of galaxy morphology classifications for various scientific purposes (Ackermann et al. 2018; Tang et al. 2019; Domínguez Sánchez et al. 2019).

In practice, we attached a two-class sigmoid classifier (0: non-spirals vs. 1: spirals) to the Xception model (Chollet 2016) trained with the ImageNet data-set beforehand (Russakovsky et al. 2014). Xception is a modern architecture of a convolutional neural network (CNN; Lecun et al. 1998; Lecun et al. 2015) developed from the Inception architecture known as GoogLeNet (Simonyan and Zisserman 2014). Throughout this study, we applied the deep learning model using TensorFlow (version 2.2.0; Abadi et al. 2016) and Keras (version 2.3.0; Chollet et al. 2015), under a single GPU, NVIDIA TITAN RTX. When we seeded random number generators built into programs, we adopted a fixed seed number of 30. While different initial setups such as random seeds and GPUs would trigger a negligible mismatch ($\lesssim 10$ percent, as far as we can ascertain) of spiral galaxy classification among models, the statistical trends discussed in this paper will not change (see, e.g., Pietrowski et al. 2021 about hardware-derived

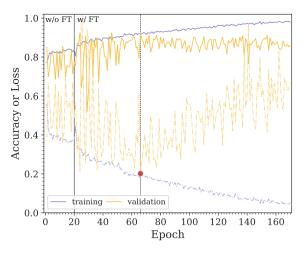


Fig. 4. Training histories of the model accuracy (Eq. 2; solid lines) and binary cross-entropy loss (Eq. 3; dot-dash lines). The purple and yellow lines depict records for the training and validation data, respectively. We started the model training without the fine-tuning (FT), and then switch to that with the FT since 20 epochs (the black solid vertical line). We employ the model in the 66th epoch (the black dotted vertical line) that has minimum validation loss as represented by the red circle.

uncertainties).

An outline of the model architecture is presented in Fig. 3. The classifier passes through dense layers (linear transformation), batch normalization (Ioffe and Szegedy 2015), and ReLU activation ($\equiv max(0, x)$; Glorot et al. 2011), and then outputs the probability value ($\hat{y} = [0:1]$) through a sigmoid function. All the HSC images are resized from 64×64 to 160×160 pixels to tailor the input size to the requirement of the Xception architecture (Chollet 2016). Also, for the same reason, our one-channel gray-scale data are distributed to all three color channels (Fig. 3), and their pixel values are standardized in each channel by the same values used in the pre-training with the ImageNet (Chollet 2016). The training data are transferred to the Xception model with data augmentation built in the Keras library (ImageDataGenerator; Fig. 3), which performs random image rotation (< 90 degrees), as well as horizontal and vertical flips.

3.2 Model training

For the model training, we employ i-band magnitude limited galaxies (i < 22.5) from the HSC-SSP DUD layer (Aihara et al. 2019), which have counterparts to the Galaxy Zoo Hubble sources at z = 0.2–0.7 within 1 arcsec radius (Willett et al. 2017). We construct their grayscale cutouts in the same manner as the primary data from the HSC-SSP Wide layer, but the imaging depths of the DUD layer used in this work are by 1.5 mag deeper than those of the Wide layer. The Galaxy Zoo Hubble of-

² https://hsc-release.mtk.nao.ac.jp/hscMap-pdr2/app/

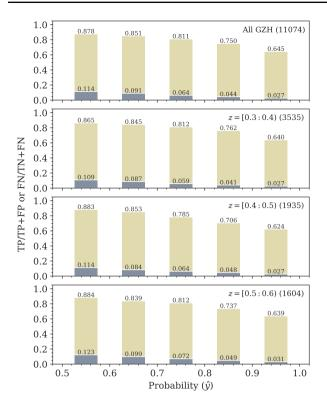


Fig. 5. The precision (yellow) and false detection fraction among non-spirals (gray) for the test data given the probability thresholds (the top panel) and those breakdown at three redsfhit bins of $z=[0.3\!:\!0.4), [0.4\!:\!0.5),$ and $[0.5\!:\!0.6)$ (the 2nd–4th rows). The precision is defined as the fraction of spirals correctly classified in the entire spiral sample, while the false detection rate means the fraction of non-spirals classified as spirals mistakingly in the non-spiral sample. This work adopts $\hat{y}=0.9$ as the selection threshold of spiral galaxies.

fers galaxy morphological classification conducted by volunteers for the images taken by the ACS camera on the Hubble Space Telescope (HST), which has 6.4 times better seeing FWHM (0.11 arcsec) than our seeing-matched HSC data (0.7 arcsec). They thus inform us of more reliable morphology information on the poorly-resolved HSC images used in this work. Following the selection procedure and thresholds of previous selection tasks suggested by Willett et al. (2017), section 6 and table 11, we select 11 074 galaxies for the model training and validation, out of which 2060 and 9014 sources are classified as spirals and non-spirals with the final weighted votes > 20. The spiral galaxy sample consists of 2049 normal spirals and 11 clumpy spirals (spiral_weighted_fraction>0.5), and the non-spiral sample contains 8466 smooth objects (smooth_best_fraction>0.5), 455 edge-on galaxies (edgeon_weighted_fraction>0.5), and 149 nonspirals with non-smooth features such as disks and clumps (no_spiral_weighted_fraction>0.5; see the literature for detailed information).

By using the classification flags defined above, we per-

formed the model training with the training data of spirals and non-spirals (N=1648 for each) and their validation data (N=412 for each). We use all spiral galaxies but randomly select 2060 non-spiral galaxies from their whole sample to maintain the same sample size as spirals. Training histories of model accuracy and binary cross-entropy loss are summarized in Fig. 4. The model accuracy is defined as:

$$accuracy \equiv \frac{TP + TN}{TP + TN + FP + FN}, \tag{2}$$

where TP (or TN) and FP (or FN) represent the numbers of true positive (or negative) and false positive (or negative), respectively. The former refers to the number of predictions where the classifier correctly predicts the positive (or negative) class as positive (or negative), respectively. However, the latter refers to the number of failed predictions. The binary cross-entropy loss is described in the following,

$$loss \equiv -y \log \hat{y} - (1 - y) \log(1 - \hat{y}), \tag{3}$$

where y and \hat{y} represent the target value $\{0,1\}$ and the probability of spirals [0:1], respectively.

We trained the model 170 times, i.e. 170 epochs, with fine-tuning since the 20th epoch. We then selected the best set of weight parameters exhibiting the least cross-entropy loss in the validation data. In the first 20 epochs, we trained only the weights of the classification head using the pre-trained CNN as feature extractor, and then trained the weights of all the layers of the deep learning model (so-called fine-tuning technique; Fig. 4). The parameter tuning was performed by Adam optimizer, an adaptive learning rate optimization algorithm (Kingma and Ba 2014), through the stochastic mini-batch training with a batch size of 32. The model training started with a default learning rate of $lr = 1 \times 10^{-3}$, and then a learning rate decay $(lr \rightarrow 2 \times 10^{-4})$ was applied in and after 50 epochs.

Consequently, we adopt the model in the 66th epoch (Fig. 4) that achieves 92 percent accuracy in both the training and validation data. The histograms in Fig. 5 summarize precision (completeness) values and fractions of false detection (contamination) against the probability for the test data with our final model. Here we reproduced the gray-scale images of the Galaxy Zoo Hubble sources from the HSC-SSP Wide layers that we actually use in the main analysis, which amounts to 11 074 objects. We then treat them as the test data-set separately from the training and validation data. Comparison examples of HST images of the test data with those in the HSC-SSP Wide layer, including obtained probability values, are shown in Fig. 6. The figure indicates that most of the test samples are successfully classified as labeled in the Galaxy

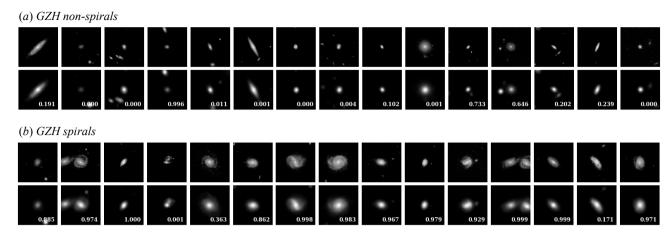


Fig. 6. Comparisons with visual classifications by Galaxy Zoo Hubble (GZH; Willett et al. 2017). From the top, figures present examples of (a) non-spiral and (b) spiral galaxies in GZH. In each figure, upper and lower panels show the gray-scale images from the COSMOS HST/ACS data (Koekemoer et al. 2007) and from the HSC-SSP Wide layer with arcsinh normalization (see §2.3), respectively. The probability values of spirals predicted by our deep learning model are represented at the bottom-right corner in each image.

Table 1. Summary of the data-set. The first to the fifth columns present the data for redshift bins, effective volumes in co-Mpc³ (excluding mask areas), total sample size ($\rm M_{\star} > 5 \times 10^{10}~M_{\odot}$), number of selected spiral galaxies, and CAMIRA red sequence clusters adopted in this study (Oguri et al. 2018), respectively.

| Redshift | Volume | Total # | Spiral # | RSC # |
|-----------|-------------------|-----------|----------|-------|
| [0.3:0.4) | 5.5×10^7 | $51\ 192$ | 16729 | 352 |
| [0.4:0.5) | 8.2×10^7 | 96 088 | 23 983 | 386 |
| [0.5:0.6) | 1.1×10^8 | 128 941 | 33 391 | 398 |

Zoo Hubble, even with the HSC images. We also confirm no clear redshift dependence of the selection completeness and contamination within the target redshift range (z=0.3–0.6).

For fairly selecting spiral galaxies, determining the selection cut of the probability value (\hat{y}) is a trade-off between the selection completeness and contamination rate, which depend on the intrinsic spiral fraction. When assuming a 30 percent spiral fraction, for instance, Fig. 5 suggests that we will have 20 percent of the contamination rate, while we can achieve nearly 90 percent completeness of the HST-based spiral galaxies. This work decides to use $\hat{y}=0.9$ as the selection threshold of spiral galaxies to reduce the contamination fraction.

3.3 Selection of spiral galaxies

Based on the constructed model, we search for spiral galaxies from 276 220 stellar-mass limited samples (§2.1). We selected galaxies with probability values greater than $\hat{y} > 0.9$ as spiral galaxies to reduce the contaminant fraction (§3.2). Consequently, 74 103 objects are classified as spiral galax-

ies, which represent 27 percent of the entire sample. The numbers of selected spirals and the effective survey volume in three redshift slices are summarized in Table 1. Also, randomly assigned 240 postage stamps of spiral galaxies in each redshift bin are presented in Fig. 7.

When assuming the completeness and contamination rates inferred from the Galaxy Zoo Hubble (§3.2 and Fig. 5), the corrected spiral fractions at z = 0.3-0.6 are estimated to be 37-49 percent. These fractions broadly agree with those suggested based on the images taken from the HST/ACS (Tasca et al. 2009, section 4), where $f_{\rm spiral} \sim$ 0.4–0.6 in the similar stellar mass limit. Thus, we consider that our deep learning model can reasonably select spiral galaxies in the corresponding redshift spaces, despite poorer spatial resolution of the HSC images than that of the HST data. However, we should still be missing significant fractions of spiral galaxies, especially at higher redshift bins, because the HST-based training and validation data would be incomplete. We note that this study does not aim to derive the intrinsic spiral fraction. Rather, we solely focus on systematic comparisons between the spiral fraction and the large-scale galaxy overdensity based on a stacking analysis, by leveraging survey volumes that are significantly larger than those in previous studies at the similar redshift range.

On top of that, we verified the precision of the photometric redshift measurement by Mizuki (Tanaka 2015) for spiral galaxies in the target redshift range z=[0.3:0.6). It is expected that photometric redshift errors of spiral galaxies would be larger than those of the entire sample because late-type galaxies tend to be bluer (i.e., less prominent Balmer break features) in the rest-frame optical wavelength. With this motivation, we utilize 32 939 galaxies

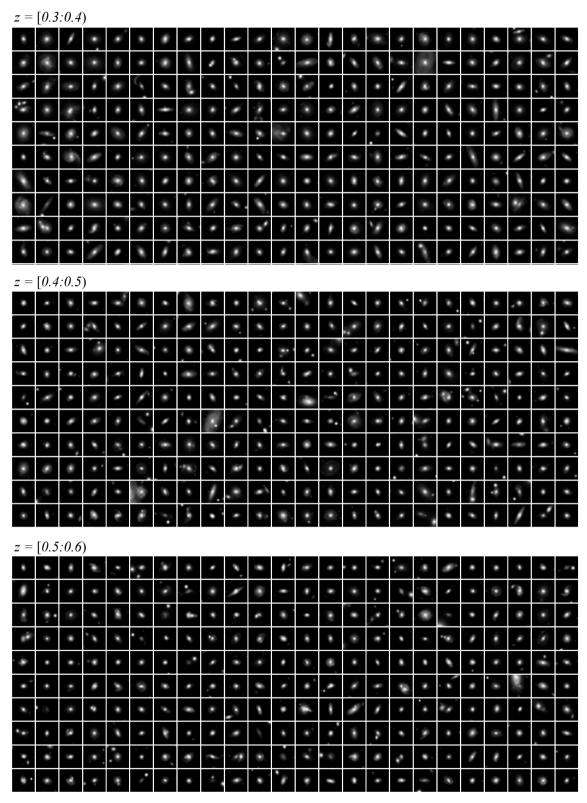


Fig. 7. From top to bottom, 240 random examples of gray-scale images classified as spiral galaxies in each redshift bin between z=0.3 and z=0.6 from the HSC-SSP Wide layer.

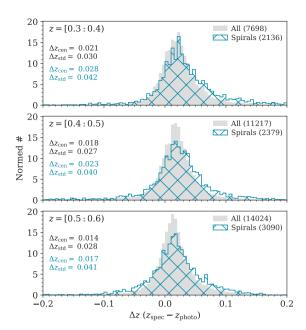


Fig. 8. Normalized distributions of differentials between spectroscopic redshifts and photometric redshifts (Δz) of the targets (gray) and selected spirals (cyan crosshatch) with spec-z at three redshift bins of z=[0.3:0.4), [0.4:0.5), and [0.5:0.6). Biweight centers $(\Delta z_{\rm cen})$ and standard deviations $(\Delta z_{\rm std})$ at each redshift bin for the entire sample and spiral galaxies are respectively illustrated by black and cyan colors in each panel.

from our sample with spectroscopic redshifts, out of which 7605 sources are classified as spirals, to verify the photo-z accuracy between spirals and the total sample. Their spectroscopic redshifts are based on various surveys available in the HSC-SSP PDR2 (Aihara et al. 2019, §5.4): SDSS DR12–14 (Alam et al. 2015; Albareti et al. 2017; Abolfathi et al. 2018), GAMA DR2 (Liske et al. 2015), PRIMUS (Coil et al. 2011; Cool et al. 2013), VIPERS (Garilli et al. 2014), VVDS (Le Fèvre et al. 2013), WiggleZ (Drinkwater et al. 2010), and zCOSMOS (Lilly et al. 2009).

Spectroscopic redshifts against photo-z for both the entire spec-z references and selected spirals are illustrated in Fig. 8. The figure suggests that spiral galaxies would exhibit slightly larger photo-z errors (by a factor of ~ 1.5) at each redshift bin, while their redshift distributions are broadly consistent with each other. Given the adequate amount of the spiral sample at each redshift bin (N > 15 000; Table 1), this study ignores such a small increase of the redshift uncertainty hereafter.

4 Large-scale environmental dependence

Based on the result of our deep-learning-based spiral classification and the density measurements from the literature (Shimakawa et al. 2021; Oguri et al. 2018), we investigate whether or not there is a large-scale morphology-density

relation (§4.1). We also study distributions of the restframe u-r colors of spirals in different density environments (§4.2).

4.1 Spiral fractions across large-scale environments

With 74 103 spiral galaxies out of 276 220 stellar-mass limited samples (Table 1), we estimate the spiral fractions in different overdensities and red sequence clusters from the archive catalog (Shimakawa et al. 2021; Oguri et al. 2018, see Section 2.2), at three target redshift bins, z = [0.3:0.4), [0.4:0.5), and [0.5:0.6). The result is represented in Fig. 9, where we stacked all sources and spirals given the similar overdensity $\Delta \sigma_{\rm r=10cMpc} = 1$ across the entire survey field to accumulate the sufficient sample size in each bin. The red diamonds also indicate the spiral fractions in the vicinity of red sequence clusters selected by the CAMIRA cluster catalog within the same survey field (Oguri et al. 2018) at the same redshift bin in each panel. Typical overdensities $(\sigma_{r=10cMpc})$ of red-sequence clusters in Shimakawa et al. (2021) are $\sigma_{r=10cMpc} = 1.1$, 0.9, and 1.1 at z = [0.3:0.4), [0.4:0.5), and [0.5:0.6), respectively. We selected galaxies in 2 co-Mpc projected distances from the red sequence clusters. The distance threshold was decided considering that the excess of red fractions has been detected within $\lesssim 2$ co-Mpc around the CAMIRA clusters (Nishizawa et al. 2018, §5.2). Fig. 9 shows both the spiral fractions from direct measurements and those with corrections of the completeness and contamination rates given in Fig. 5. The contamination rates within the selected spirals are estimated to be approximately 5–8 percent.

Owing to the combination of the wide-field deep imaging data by HSC-SSP and the deep learning classification, Fig. 9 successfully demonstrates moderate trends of the large-scale environmental dependence of the spiral fraction at z=0.3–0.6 related to lower spiral fractions at higher overdensities on 10 co-Mpc scale. What is worth noting is that we find a systematic increase of the spiral fraction in lower-density environments at each redshift slice, which is achievable only with such continuous overdensity information by our previous work (Shimakawa et al. 2021). Moreover, we confirmed deficits of the spiral fraction in the vicinity of red sequence clusters at all three redshift bins, as reported in previous studies (e.g., Moran et al. 2007; Poggianti et al. 2009 and references therein).

4.2 Rest-frame colors of spirals vs environments

Then, we investigated the color dependence of detected spiral galaxies on the galaxy overdensity. Their rest-frame u-r colors are derived by the SED-based fitting

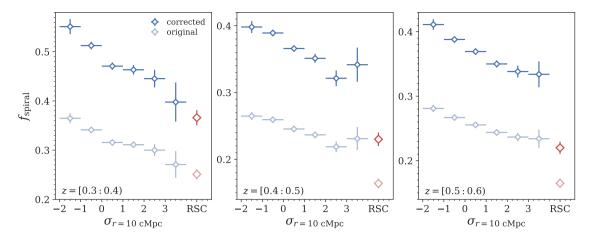


Fig. 9. From left to right, spiral fractions as a function of the over-density at redshift bins of z = [0.3:0.4), [0.4:0.5), and [0.5:0.6), respectively. The red symbol in the far right in each panel depicts the spiral fraction in the vicinity (< 2 co-Mpc) of red sequence clusters (RSC) from Oguri et al. (2018). Vertical error bars indicate Poisson errors. The light color symbols are based on direct measurements with the selection threshold of the probability $\hat{y} = 0.9$, and the dark color symbols are scaled from the original values based on the completeness and contamination rates of the spiral classification inferred from the test data (see §3.2 and Fig. 5).

code, Mizuki (Tanaka 2015). This is motivated by the well-known environmental dependence of the red fraction (e.g., Tanaka et al. 2005; Peng et al. 2010; Alpaslan et al. 2015). In particular, many previous studies have reported that passive spiral galaxies (so-called anemic spirals; van den Bergh 1976) are more frequently observed in galaxy clusters or intermediate overdensities (e.g. Goto et al. 2003a; Boselli and Gavazzi 2006; Blanton and Moustakas 2009; Bamford et al. 2009; Masters et al. 2010 and references therein). Similar to those already observed in the past, there could be a color dependency of spiral galaxies even on large-scale environments.

The derived rest-frame u-r color distributions of spiral galaxies as a function of the overdensity are illustrated in Fig. 10. Dashed lines and red error bars represent 68th percentiles of spiral galaxies given overdensity and red sequence clusters, respectively. We observe bluer color distributions of spiral galaxies compared to those in the entire sample except the lowest-z sample at z = [0.3:0.4). However, the similar colors between spirals and all sources at z = [0.3:0.4) should be due to a technical issue since the HSC filters (grizy) do not fully cover the rest-frame uband photometry of galaxies at this redshift range. Over the redshift range of z = 0.3-0.6, in general, we cannot determine any significant color dependence on the largescale over-density given the spiral sample, while there is a lack of relatively bluer spirals in the highest density bin and clusters at z = [0.3:0.4) (Fig. 10). A possible explanation of a decorrelation between rest-frame u-r colors of spirals and the galaxy overdensities is described in the discussion section (§5). On the other hand, median u-rcolors of spirals in the vicinity of red sequence clusters are

slightly redder than those in the other fields at z = [0.4:0.5) and z = [0.5:0.6), which broadly agrees with the observational trends reported in the previous work (Goto et al. 2004; Wolf et al. 2007; Bamford et al. 2009; Cantale et al. 2016).

5 Discussion

We discuss and attempt to interpret the results obtained in the last section. Based on the stacking analysis, we determined a statistical trend in which the spiral fraction tends to increase (or decrease) in lower (or higher) densities at z=0.3–0.6 on ten co-Mpc scales. This suggests a bias on the global scale across the large-scale structure of the universe, which could originate from a difference in mass assembly histories in the underlying density environments of the large-scale structure. In fact, it is plausible that the known morphology–density relation in and around massive clusters can be validated even on such a wide scale, because large-scale overdensities tend to be associated with larger numbers of clusters, as demonstrated in the study by Shimakawa et al. (2021).

Moderate environmental dependence of galaxy morphology on the large-scale will lead to a non-negligible cosmic variance in the measurement of the spiral fraction if research does not use the data covering sufficiently large areas. For testing such a cosmic variance effect, we investigate the variation of the spiral fraction in individual fields given survey areas at each redshift bin. Fig. 11 represents the variance of the spiral fractions ($f_{\rm spiral}$) within 1 and 27 deg² based on 1000 random points in our survey field, where 27 deg² corresponds to the footprint of

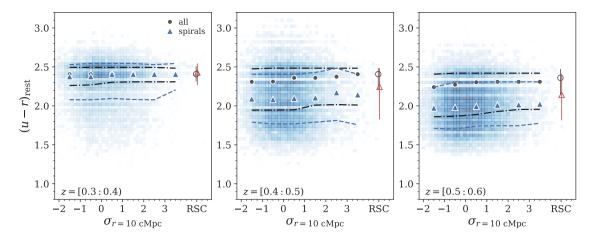


Fig. 10. Distributions of the rest-frame u-r colors of the entire sample and spiral galaxies as a function of the galaxy over-density ($\sigma_{\rm r=10cMpc}$). Black-filled circles and dot-dash lines represent the median and 68th percentiles for the entire source, and blue triangles and dash lines show those for the spirals. The black open circles and red open triangles are massive galaxies and spirals nearby red sequence clusters (Oguri et al. 2018). The error bars indicate 68th percentile regions. We note that the similar color distributions of spirals to the entire sample at z=0.3–0.4 should be due to the measurement error because their rest-frame u-band fluxes are not fully covered by the HSC grizy filters.

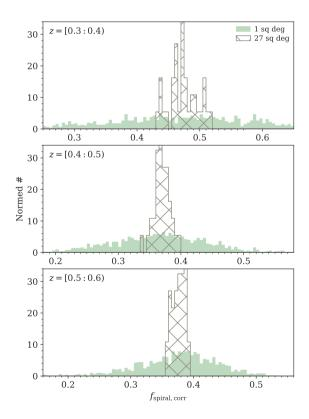


Fig. 11. Normalized distributions of the corrected spiral fractions in random 1 deg² (light green filled) and 27 deg² (dark green crosshatch) fields at z = [0.3:0.4), [0.4:0.5), and [0.5:0.6).

the HSC-SSP DUD layer. The figure suggests a significant cosmic variance in the derivation of the spiral fraction in 1 deg². However, measurement errors due to the small sample size $(N = 182, 341, \text{ and } 457 \text{ per deg}^2 \text{ on average at})$ z = [0.3:0.4), [0.4:0.5), and [0.5:0.6)) would contribute to some increase of the variance. Even if the survey area reaches 27 deg², there are small variations of ± 0.02 to 0.04 depending on the redshift. The significant variability also cautions that, when we study morphology-density dependence on the local scale, we may need to take care of the underlying large-scale structure of the target region. Such comprehensive work requires an expensive spectroscopic survey with extremely wide-field coverage, such as DESI (DESI Collaboration et al. 2016), PFS (Takada et al. 2014; Tamura et al. 2016), and 4MOST (de Jong et al. 2012; de Jong et al. 2019). These programs will allow us to unveil a systematic bias of the spiral fraction in various environments on a large scale as well as the local scale.

Next, selected spiral objects do not exhibit a clear environmental dependence on the rest-frame u-r color. Previous studies have reported that galaxy clusters and/or groups tend to have a higher fraction of red spirals (Goto et al. 2003b; Wolf et al. 2007; Bamford et al. 2009; Masters et al. 2010), thus suggesting a transition of spiral galaxies falling into massive halos to S0 galaxies, as observed in today's massive clusters (Goto et al. 2004; Moran et al. 2007; Kovač et al. 2010). We reconfirm such a systematic color trend in the vicinity of red sequence clusters in our sample. However, regarding large-scale environments (10 co-Mpc in our case), such a physical transition occurring on the local scale (\sim a physical Mpc) becomes negligible, which might explain the absence of a significant trend in

this study.

We should stress that the current spiral classification is highly limited to bright and massive objects with a limiting stellar mass of $5 \times 10^{10}~{\rm M}_{\odot}$. Also, we would miss a non-negligible fraction of spiral galaxies owing to the resolution limit (0.7 arcsec in seeing FWHM), though we used the HST-based morphological information as classification flags by Willett et al. (2017). Such a selection bias is a major challenge that needs to be addressed in the future, as stated at the end.

6 Conclusions

Lastly, we summarize the flow of this paper. We investigated the spiral fraction of mass-limited galaxies based on the sample in the significant volumes obtained from the HSC-SSP PDR2. This study attempted to elucidate the global-scale environmental dependence that may originate from the varying growth of underlying density environments for the large-scale structure rather than physical interactions between galaxies and clusters occurring on the local scale. Previous studies, such as the SED fitting (Tanaka et al. 2018), projected density map (Shimakawa et al. 2021), and red sequence cluster search (Oguri et al. 2018) based on HSC-SSP, enabled us to achieve such an objective. Consequently, we obtained 276 220 massive galaxies across 360 deg², parts of which are associated with 1136 red sequence clusters at the corresponding redshift range. A total of 74 103 galaxies were labeled as spiral galaxies via transfer learning based on a pre-trained deep CNN. The obtained results indicate the moderate large-scale environmental dependence of the spiral fraction at z = 0.3-0.6. Furthermore, we do not observe any obvious trend of the rest-frame u-r colors for the spiral galaxies towards the overdensity. These results suggest a large-scale environmental dependence of galaxy morphology at least up to z = 0.6, while observed color transitions of spiral galaxies falling into galaxy clusters and groups are no longer detected on such a wide scale.

Although the current analysis is limited by the photo-z uncertainty and high stellar mass ($>5\times10^{10}~\rm M_{\odot}$), ongoing and upcoming intensive programs will resolve these limitations. For instance, DESI (DESI Collaboration et al. 2016) will address more than a thousand spectroscopic data per square degree for emission-line galaxies at intermediate redshift ($z\lesssim1.3$) over $14k~\rm deg^2$. Other forthcoming spectroscopic surveys such as PFS (Takada et al. 2014; Tamura et al. 2016), MOONS (Cirasuolo et al. 2011; Cirasuolo et al. 2014), and 4MOST (de Jong et al. 2012; de Jong et al. 2019) will also facilitate the accumulation of more detailed redshift information. In addition, wide-field high-

resolution imaging by the Roman Space Telescope (Spergel et al. 2015; Akeson et al. 2019) will provide a clear path for the morphology classification in the distant universe, which can considerably extend the sample size towards lower stellar mass and higher redshift from this study.

Acknowledgments

This study was conducted based on data collected at the Subaru Telescope and retrieved from the HSC data archive system, which is operated by Subaru Telescope and Astronomy Data Center at National Astronomical Observatory of Japan. We are honored and grateful for the opportunity of observing the Universe from Maunakea, which has cultural, historical, and natural significance in Hawaii. All the data underlying this publication are available under the Second Public Data Release of Hyper Suprime-Cam Subaru Strategic Program (https://hsc.mtk.nao.ac.jp/ssp/data-release/)

The Hyper Suprime-Cam (HSC) collaboration includes the astronomical communities of Japan and Taiwan, and Princeton University. The HSC instrumentation and software were developed by the National Astronomical Observatory of Japan (NAOJ), the Kavli Institute for the Physics and Mathematics of the Universe (Kavli IPMU), the University of Tokyo, the High Energy Accelerator Research Organization (KEK), the Academia Sinica Institute for Astronomy and Astrophysics in Taiwan (ASIAA), and Princeton University. Funding was contributed by the FIRST program from Japanese Cabinet Office, the Ministry of Education, Culture, Sports, Science and Technology (MEXT), the Japan Society for the Promotion of Science (JSPS), Japan Science and Technology Agency (JST), the Toray Science Foundation, NAOJ, Kavli IPMU, KEK, ASIAA, and Princeton University.

This paper makes use of software developed for the Large Synoptic Survey Telescope. We thank the LSST Project for making their code available as free software at http://dm.lsst.org

The Pan-STARRS1 Surveys (PS1) have been made possible through contributions of the Institute for Astronomy, the University of Hawaii, the Pan-STARRS Project Office, the Max-Planck Society and its participating institutes, the Max Planck Institute for Astronomy, Heidelberg and the Max Planck Institute for Extraterrestrial Physics, Garching, The Johns Hopkins University, Durham University, the University of Edinburgh, Queen's University Belfast, the Harvard-Smithsonian Center for Astrophysics, the Las Cumbres Observatory Global Telescope Network Incorporated, the National Central University of Taiwan, the Space Telescope Science Institute, the National Aeronautics and Space Administration under Grant No. NNX08AR22G issued through the Planetary Science Division of the NASA Science Mission Directorate, the National Science Foundation under Grant No. AST-1238877, the University of Maryland, and Eotvos Lorand University (ELTE) and the Los Alamos National Laboratory.

Funding for the Sloan Digital Sky Survey IV has been provided by the Alfred P. Sloan Foundation, the U.S. Department of Energy Office of Science, and the Participating Institutions. SDSS-IV acknowledges support and resources from the Center for High Performance Computing at the University of Utah.

The SDSS website is www.sdss.org.

We thank anonymous referee for helpful feedback. We would like to thank Editage (www.editage.com) for English language editing. This work was partially supported by Summer Student Program (2020) National Astronomical Observatory of Japan and the Department of Astronomical Science, The Graduate University for Advanced Studies, SOKENDAI.

This study made extensive use of the following tools, NumPy (Harris et al. 2020), the Tool for OPerations on Catalogues And Tables, TOPCAT (Taylor 2005), a community-developed core Python package for Astronomy, Astropy (Astropy Collaboration et al. 2013), and Python Data Analysis Library pandas (McKinney et al. 2010).

References

Abadi, M., et al. 2016, arXiv e-prints, arXiv:1603.04467

Abazajian K., et al. 2004, AJ, 128, 502

Abolfathi, B., et al. 2018, ApJS, 235, 42

Ackermann, S., et al. 2018, MNRAS, 479, 415

Aihara, H., et al. 2018, PASJ, 70, S4

Aihara, H., et al. 2019, PASJ, 71, 114

Akeson, R., et al. 2019, arXiv e-prints, arXiv:1902.05569

Alam, S., et al. 2015, ApJS, 219, 12

Albareti, F. D., et al. 2017, ApJS, 233, 25

Alpaslan, M., et al. 2015, MNRAS, 451, 3249

Astropy Collaboration, Robitaille, et al. 2013, A&A, 558, A33

Baldry, I. K., et al. 2006, MNRAS, 373, 469

Balogh, M. L., et al. 2004, ApJL, 615, L101

Bamford, S. P., et al. 2009, MNRAS, 393, 1324

Banerji, M., et al. 2010, MNRAS, 406, 342

Bekki, K., & Couch, W. J. 2011, MNRAS, 415, 1783

Blanton, M. R., & Moustakas, J. 2009, ARA&A, 47, 159

Bosch, J., et al. 2018, PASJ, 70, S5

Boselli, A., & Gavazzi, G. 2006, PASP, 118, 517

Bower, R. G., Lucey, J. R., & Ellis, R. S. 1992, MNRAS, 254, 601

Bower, R. G., Kodama, T., & Terlevich, A. 1998, MNRAS, 299, 1193

Bozinovski, S., & Fulgosi, A. 1976, Proc. Symp. Informatica 3-121-5

Brough, S., et al. 2017, ApJ, 844, 59

Butcher, H., & Oemler, A. 1984, ApJ, 285, 426

Cantale, N., et al. 2016, A&A, 589, A82

Capak, P., et al. 2007, ApJS, 172, 284

Cappellari, M., et al. 2011, MNRAS, 416, 1680

Chabrier, G. 2003, PASP, 115, 763

Cheng, T.-Y., et al. 2020, MNRAS, 493, 4209

Chollet, F., et al. 2015, Available at: https://keras.io

Chollet, F. 2016, arXiv e-prints, arXiv:1610.02357

Cirasuolo, M., et al. 2011, The Messenger, 145, 11

Cirasuolo, M., et al. 2014, Proc. SPIE, 9147, 91470N

Coil, A. L., et al. 2011, ApJ, 741, 8

Cool, R. J., et al. 2013, ApJ, 767, 118

Cooper, M. C., et al. 2007, MNRAS, 376, 1445

Costa-Duarte, M. V., et al. 2018, MNRAS, 478, 1968

Couch, W. J., et al. 1998, ApJ, 497, 188

Coupon, J., et al. 2018, PASJ, 70, S7

Davidzon, I., et al. 2017, A&A, 605, A70

Davis, M., et al. 1985, ApJ, 292, 371

de Jong, R. S., et al. 2012, Proc. SPIE, 8446, 84460T

de Jong, R. S., et al. 2019, The Messenger, 175, 3

de Vaucouleurs, G. 1961, ApJS, 5, 233

Dekel, A., & Silk, J. 1986, ApJ, 303, 39

DESI Collaboration, Aghamousa, et al. 2016, arXiv e-prints, arXiv:1611.00036

Dieleman, S., Willett, K. W., & Dambre, J. 2015, MNRAS, 450,

Domínguez Sánchez, H., et al. 2019, MNRAS, 484, 93

Donnari, M., et al. 2021, MNRAS, 500, 4004

Dressler, A. 1980, ApJ, 236, 351

Dressler, A., et al. 1997, ApJ, 490, 577

Drinkwater, M. J., et al. 2010, MNRAS, 401, 1429

Fogarty, L. M. R., et al. 2014, MNRAS, 443, 485

Furusawa, H., et al. 2018, PASJ, 70, S3

Garilli, B., et al. 2014, A&A, 562, A23

Ghosh, A., et al. 2020, ApJ, 895, 112

Gladders, M. D., & Yee, H. K. C. 2005, ApJS, 157, 1

Glorot, X., Bordes, A., & Bengio. Y. 2011, In Proc. 14th International Conf. on Artificial Intelligence and Statistics, 315, 323

Goto, T., et al. 2003, MNRAS, 346, 601

Goto, T., et al. 2003, PASJ, 55, 757

Goto, T., et al. 2004, MNRAS, 348, 515

Goto, T. 2005, MNRAS, 356, L6

Greene, J. E., et al. 2017, ApJL, 851, L33

Grützbauch, R., et al. 2011, MNRAS, 411, 929

Guzzo, L., et al. 2007, ApJS, 172, 254

Harris, C. R., et al. 2020, Nature, 585, 357Hashimoto, T., et al. 2019, MNRAS, 489, 2014

Hinshaw, G., et al. 2013, ApJS, 208, 19

Holden, B. P., et al. 2007, ApJ, 670, 190

Houghton, R. C. W., et al. 2013, MNRAS, 436, 19

Hunter, J. D. 2007, Computing in Science and Engineering, 9, 90

Ilbert, O., et al. 2010, ApJ, 709, 644

Ioffe, S., & Szegedy, C. 2015, arXiv e-prints, arXiv:1502.03167

Joshi, G. D., et al. 2020, MNRAS, 496, 2673

Kauffmann, G., et al. 2004, MNRAS, 353, 713

Kawanomoto, S., et al. 2018, PASJ, 70, 66

Kereš, D., et al. 2005, MNRAS, 363, 2

Kingma, D. P., & Ba, J. 2014, arXiv e-prints, arXiv:1412.6980

Kodama, T., et al. 2007, MNRAS, 377, 1717

Koekemoer, A. M., et al. 2007, ApJS, 172, 196

Komiyama, Y., et al. 2018, PASJ, 70, S2

Koulouridis, E., et al. 2021, A&A, 652, A12

Kovač, K., et al. 2010, ApJ, 718, 86

Kuminski, E., & Shamir, L. 2016, ApJS, 223, 20

Laigle, C., et al. 2016, ApJS, 224, 24

Larson, R. B., Tinsley, B. M., & Caldwell, C. N. 1980, ApJ, 237, 692

Lecun Y., et al. 1998, Proc. IEEE, 86, 2278

Lecun, Y., Bengio, Y., & Hinton, G. 2015, Nature, 521, 436

Le Fèvre, O., et al. 2013, A&A, 559, A14

Lietzen, H., et al. 2012, A&A, 545, A104

Lilly, S. J., et al. 2009, ApJS, 184, 218

Liske, J., et al. 2015, MNRAS, 452, 2087

Lupton, R. H., Gunn, J. E., & Szalay, A. S. 1999, AJ, 118, 1406

Lupton, R., et al. 2004, PASP, 116, 133

Masters, K. L., et al. 2010, MNRAS, 405, 783

Maturi, M., et al. 2019, MNRAS, 485, 498

McKinney W., et al. 2010, Proc. 9th Python Sci. Conf., 1697900, 51

Mei, S., et al. 2009, ApJ, 690, 42

Miyazaki, S., et al. 2018, PASJ, 70, S1

Moore, B., Lake, G., & Katz, N. 1998, ApJ, 495, 139

Moran, S. M., et al. 2007, ApJ, 671, 1503

Muzzin, A., et al. 2008, ApJ, 686, 966

Muzzin, A., et al. 2014, ApJ, 796, 65

Nishizawa, A. J., et al. 2018, PASJ, 70, S24

Oguri, M. 2014, MNRAS, 444, 147

Oguri, M., et al. 2018, PASJ, 70, S20

Oke, J. B., & Gunn, J. E. 1983, ApJ, 266, 713

Old, L. J., et al. 2020, MNRAS, 493, 5987

Peng, Y.-. jie., et al. 2010, ApJ, 721, 193

Peng, Y.-. jie., et al. 2012, ApJ, 757, 4

Pietrowski, M., et al. 2021, arXiv e-prints, arXiv:2109.01451

Poggianti, B. M., et al. 2006, ApJ, 642, 188

Poggianti, B. M., et al. 2009, ApJL, 697, L137

Postman, M., et al. 2005, ApJ, 623, 721

Pratt L. Y., et al. 1993, in Advances in Neural Information Proc. Systems 5, 204

Rood, H. J., & Sastry, G. N. 1971, PASP, 83, 313

Russakovsky, O., et al. 2014, arXiv e-prints, arXiv:1409.0575

Rykoff, E. S., et al. 2014, ApJ, 785, 104

Schawinski, K., et al. 2014, MNRAS, 440, 889

Scoville, N., et al. 2007, ApJS, 172, 1

Shimakawa, R., et al. 2021, MNRAS,

Simonyan, K., & Zisserman, A. 2014, arXiv e-prints, arXiv:1409.1556

Skibba, R. A., et al. 2009, MNRAS, 399, 966

Smith, G. P., et al. 2005, ApJ, 620, 78

Somerville, R. S., & Davé, R. 2015, ARA&A, 53, 51

Spergel, D., et al. 2015, arXiv e-prints, arXiv:1503.03757

Szalay, A., et al. 2001, arXiv e-prints, cs/0111015

Tadaki, K.-. ichi., et al. 2020, MNRAS, 496, 4276

Takada, M., et al. 2014, PASJ, 66, R1

Tamura, N., et al. 2016, Proc. SPIE, 9908, 99081M

Tan, C., et al. 2018, arXiv e-prints, arXiv:1808.01974

Tanaka, M., et al. 2005, MNRAS, 362, 268

Tanaka, M. 2015, ApJ, 801, 20

Tanaka, M., et al. 2018, PASJ, 70, S9

Tang, H., Scaife, A. M. M., & Leahy, J. P. 2019, MNRAS, 488, 3358

Tasca, L. A. M., et al. 2009, A&A, 503, 379

Taylor, M. B. 2005, Astronomical Data Analysis Software and Systems XIV, 347, 29

Terlevich, A. I., Caldwell, N., & Bower, R. G. 2001, MNRAS, 326, 1547

van den Bergh, S. 1976, ApJ, 206, 883

van der Wel, A. 2008, ApJL, 675, L13

Veale, M., et al. 2017, MNRAS, 471, 1428

Visvanathan, N., & Sandage, A. 1977, ApJ, 216, 214

Vulcani, B., et al. 2011, MNRAS, 412, 246

Wetzel, A. R., Tinker, J. L., & Conroy, C. 2012, MNRAS, 424, 232

Wetzel, A. R., et al. 2013, MNRAS, 432, 336

White, S. D. M., et al. 2005, A&A, 444, 365

White, S. D. M., & Frenk, C. S. 1991, ApJ, 379, 52

Willett, K. W., et al. 2017, MNRAS, 464, 4176

Wolf, C., et al. 2007, MNRAS, 376, L1

Wolf, C., et al. 2009, MNRAS, 393, 1302

York, D. G., et al. 2000, AJ, 120, 1579

Zhu, X.-P., et al. 2019, Ap&SS, 364, 55